



Lunar Surface and Buried Rock Abundance Retrieved from Chang'E-2 Microwave and Diviner Data

Guangfei Wei^{1,2} , Shane Byrne³ , Xiongyao Li^{1,2}, and Guoping Hu⁴¹ Center for Lunar and Planetary Sciences, Institute of Geochemistry, CAS, Guiyang, 550081, People's Republic of China; gfwei0554@gmail.com² CAS Center for Excellence in Comparative Planetology, Hefei, 230026, People's Republic of China³ Lunar and Planetary Laboratory, University of Arizona, Tucson, AZ, 85721, USA⁴ State Key Laboratory of Lunar and Planetary Sciences, Macau University of Science and Technology, Macau, People's Republic of China

Received 2020 April 9; revised 2020 August 23; accepted 2020 August 24; published 2020 October 26

Abstract

Microwave emission of the Moon, measured by the Chang'E-2 Microwave Radiometer (MRM), provides an effective way to understand the physical properties of lunar near-surface materials. The observed microwave brightness temperature is affected by near-surface temperatures, which are controlled by the surface albedo, roughness, regolith thermophysical properties, and the high thermal inertia and permittivity of both surface and buried rocks. In this study, we propose a rock model using thermal infrared measurements from the Lunar Reconnaissance Orbiter's (LRO) Diviner as surface temperature constraints. We then retrieve the volumetric rock abundance (RA) from nighttime MRM data at several rocky areas. Although our retrieved MRM RA cannot be compared to the rock concentration measured with LRO Camera images directly, there is a good agreement with Diviner-derived RA and radar observations. The extent of several geological units, including rocky craters, hummocky regions, and impact melts, agree well with the distribution of elevated rock concentration. Based on seven large craters with published model ages, we present an inverse correlation between rock concentration and crater age. The result shows that the rock concentration decreases with crater age rapidly within 1 Ga but declines slowly after that. These data are consistent with a short survival time for exposed rocks and a long lifetime for buried rocks that are shielded from lunar surface processes.

Unified Astronomy Thesaurus concepts: [Lunar surface \(974\)](#); [Lunar geochronology \(954\)](#); [Lunar craters \(949\)](#); [Lunar evolution \(952\)](#); [Lunar science \(972\)](#); [The Moon \(1692\)](#)

1. Introduction

Lunar surface rocks provide information about the evolution of the Moon's crust and critical events such as volcanism and meteorite bombardment. Generally, four typical lunar rocks—volcanic rocks, highland pristine rocks, polymict breccia, and fragments (<1 cm)—have been found on the Moon (Taylor et al. 1991). Over the past several billion years, most lunar rocks have been shattered, crushed, melted, and/or mixed by meteoroid impacts. As a result, rocks of different sizes are exposed, protrudent, or buried as observed by the Lunar Reconnaissance Orbiter Camera (LROC; Greenhagen et al. 2016).

Infrared observations of the Moon suggest that the highly contrasting thermal inertia between rocks and soils plays a major role in surface/subsurface thermal behavior over a lunar day (Roelof 1968; Bandfield et al. 2011; Elder et al. 2017; Hayne et al. 2017). Assuming the surface rocks are a half-infinite slab, Bandfield et al. (2011) derived the global rock abundance (RA) and rock-free regolith temperatures from nighttime infrared measurements of the Lunar Reconnaissance Orbiter's (LRO's) Diviner instrument. The rock concentration in their work is defined by the areal percentage of rock slab in each pixel. However, unresolved slopes contributed to anisothermality that would be incorrectly modeled as rock concentration (Bandfield et al. 2011, 2017). Additionally, according to their modeling, the derived rock concentration is

dependent on both the rock size (>1 m in diameter) and the local time (Bandfield et al. 2011). In reality, rocks on the Moon present in different sizes and random shapes are exposed on the surface and/or buried at different depths (Roelof 1968), which could result in an underestimation of areal RA (Bandfield et al. 2011).

The highly contrasting dielectric permittivity of rocks and regolith fines also causes diurnal microwave brightness temperature (T_B) anomalies that have been observed by the Chang'E-1 and -2 (CE-1/-2) Microwave Radiometer (MRM; Chan et al. 2010; Zheng et al. 2012, 2019). Gong & Jin (2013) interpreted the nighttime T_B anomaly at a Tycho crater to be due to high values of dielectric permittivity and thermal inertia of rocks. Recently, Hu et al. (2018) developed a rock model for low- T_B craters to simulate the thermal anomalies that were revealed by CE-2 MRM data. However, these researchers attempted to calculate the soil/rock mixture thermal inertia and dielectric permittivity by employing the areal Diviner surface rock concentration instead of the volumetric rock concentrations. Consequently, this caused large uncertainties in their T_B simulation because (1) the areal coverage of surface rocks does not represent the volume of rocks directly, and (2) small rocks (<1 m in diameter) and buried fragments have not been retrieved by the Diviner rock model. In addition, the anisothermality of rocky areas influenced by surface roughness and emissivity would also cause significant uncertainties in T_B simulations. Therefore, to investigate the T_B anomalies at rocky areas in detail, additional factors, including topographic effects, the thermal properties of lunar materials, and the near-surface volumetric content of rocks, should be taken into account before interpreting the microwave observations.

One-dimensional thermal models are widely used to calculate the global surface/subsurface temperatures on the Moon. The surface temperature is a critical boundary condition for the solution of the thermal model in a lunar day, especially for rocky areas. Recently, Wei et al. (2019) proposed a new method to calculate regolith temperature profiles and to simulate microwave brightness temperatures using Diviner observations as surface thermal constraints. Specifically, Diviner's repeated observations of rocky areas provide us with data to constrain the complex surface thermal environment. Here, we continue this work by taking the volumetric rock concentration into account in T_B simulations. That is, the rock signatures, including exposed small rocks and buried fragments that have not been sensed by Diviner rock model, are considered in this study.

2. Data Sets and Method

2.1. Diviner Bolometric Brightness Temperature Data

The LRO launched on 2009 June 18 and then transitioned into a nominal mission with an average altitude ~ 50 km on 2009 June 27 (Mazarico et al. 2012). Diviner on board the LRO is the first instrument designed to systematically investigate the global surface thermal environment (Paige et al. 2010a). Diviner maps the solar reflectance and infrared emission in a push broom configuration from its nine channels. Each channel consists of an array of 21 detectors that are nominally nadir-pointing to the surface of the Moon. Channels 1 and 2 measure reflected solar radiation with identical spectral passbands of $0.35\text{--}2.8\ \mu\text{m}$ but with different sensitivities. Channels 3 through 5, with narrow spectral passband filters near $8\ \mu\text{m}$, are used to diagnose the bulk silicate mineralogy. The remaining channels (6–9) with the wavelength range of $13\text{--}400\ \mu\text{m}$ are intended to characterize the surface thermal emission over a wide range of temperatures. More details of Diviner are described in Paige et al. (2010a).

At its nominal altitude of ~ 50 km, Diviner measured the lunar surface with a spatial resolution of ~ 200 m. The data are obtained in a nearly continuous north–south circular swathes with a width of 3.4 km (Vasavada et al. 2012). Based on more than 5.5 yr of Diviner observations, Williams et al. (2017) compiled all nadir observations from 2009 July 5 to 2015 April 1, into bins of 0.5° latitude and longitude and 0.25 hr of local time. The bolometric brightness temperature, T_{Bol} , is then determined from the brightness temperatures of channels 3–9 in each bin. Notably, the spectrally integrated T_{Bol} reflects the surface heat balance directly and approximates the surface kinetic temperature (Paige et al. 2010b).

2.2. Microwave Radiometer Data

CE-2, China's second lunar orbiter, was launched on 2010 October 1. In addition to collecting high-resolution images for the following C-3 landed mission, the payloads were identical to those of its predecessor (CE-1), but CE-2 provides higher-resolution observations due to its lower altitude (~ 100 km, half of CE-1's). The MRM on board CE-2 is designed to measure the global microwave emission of the Moon (Zheng et al. 2019; Zhu et al. 2019). The MRM contains two sets of observation and calibration antennas, and each has four channels, i.e., 3, 7.8, 19.35, and 37 GHz. The spatial resolution is 25 km at 3 GHz and 17.5 km at the other frequencies. A two-point calibration method with alternating views of the lunar surface

and cold space was used to derive the microwave brightness temperature of the Moon (Wang et al. 2010b) and the pointing angle of CE-2 MRM's calibration antennas were adjusted to avoid contamination from lunar surface emissions (Feng et al. 2013).

The CE-2 MRM began to measure the lunar surface in a polar orbit on 2010 October 15. The ground station received 2401 tracks of T_B data before CE-2 left lunar orbit for the Sun–Earth Lagrange point 2 on 2011 May 20 (Zheng et al. 2019). After systematic calibration and geometric correction, the T_B data were published in the same format as CE-1's (Zheng et al. 2012). For the typical permittivity of lunar regolith, the penetration depths are $\sim 5\text{--}6$ m at 3 GHz, 2 m at 7.8 GHz, 1 m at 19.35 GHz, and <0.5 m at 37 GHz (Wang et al. 2010a). Thus, more geophysical information of near-surface materials, including buried rocks, can be revealed by lower frequencies (longer wavelengths).

In this study, we use the T_B data obtained from 7.8 and 19.35 GHz channels to investigate the thermophysical properties of regolith at greater depths where rocks and/or fragments may exist. To avoid topographic effects at high latitudes, we investigate the rocky areas in the low and middle latitudes of the Moon. In addition, we restricted the local times of CE-2 measurements we analyzed to be between 1900 and 0500 to avoid surface light scattering and cold-horn heat contamination near the terminator (Feng et al. 2019). To facilitate comparison with global T_{Bol} data, we compiled the CE-2 T_B data set into bins of $0.5^\circ \times 0.5^\circ$ latitude by longitude.

2.3. LRO Camera WAC and NAC Data

The LROC on board LRO has been successfully used to investigate meter-scale morphological features on the Moon. LROC consists of three imaging subsystems, i.e., two Narrow Angle Camera (NACs) and the multispectral Wide Angle Camera (WAC; Robinson et al. 2010). The WAC is a push-frame imager designed to provide global imaging in monochrome or color (Robinson et al. 2010). In monochrome mode at 50 km altitude, the WAC observes the ground with a single band (643 nm) at a nadir pixel scale 75 m. In color mode, images can be acquired with two ultraviolet (321–360 nm) and five visible (415–690 nm) wavelength filters through separate optics (Robinson et al. 2010). Here, the WAC images obtained in monochrome mode are used as context for the retrieved RAs.

The NAC is comprised of two cameras, designated left and right, that are designed to provide nadir viewing monochrome line-scan images of 5064 by $52,224$ pixels with $0.5\ \text{m}\ \text{pixel}^{-1}$ over a combined 5 km ground track swath from an altitude of 50 km (Robinson et al. 2010, 2016). The NAC images have been widely used to detect lunar surface morphology—for example, exposed blocks down to ~ 1 m horizontal scale with ≥ 0.5 m heights and craters with diameters ≥ 2.5 m (Bandfield et al. 2011; Basilevsky et al. 2013; Greenhagen et al. 2016; Li & Wu 2018). Recently, a series of NAC images covering several typical craters and highlands were mosaiced together to better characterize a larger range of geological units on the Moon (Klem et al. 2014). Details of NAC images used in our study are listed in Table 1.

2.4. Methodology

As described above, Diviner observations provide sufficient thermal measurements for deriving surface RA; however, the

Table 1
NAC Images Used in this Study

Image Number	Pixel Scale (m pxl ⁻¹)	Incidence (°)	Center Coordinate (°)
M1130983324LC	0.83	34.21	(131.8E, 21.8S)
M126079244LC	0.60	26.93	(130.2E, 18.8S)
The controlled mosaics, NAC ROI ARISTARCLOA E237N3125 covering Aristarchus crater combined from eight NAC frames: M1096815140L/R, M1096800850L/R, M1096807995L/R and M1096793706L/R.	1.17	67–69	(47.5S, 23.7E)
The controlled mosaics, NAC ROI HLNDPONDLOA E426N1671 covering the highland ponds are combined from 10 NAC frames: M182425021L/R, M182432168L/R, M182439316L/R, M182446463L/R and M182453611L/R.	1.70	62–63	(167.1E, 42.6N)

Diviner rock model is not sensitive to exposed small rocks (<1 m in diameter) or any buried rocks that have been detected by radar observations (Campbell 2012; Ghent et al. 2014, 2016). Microwave emission is sensitive to rocks of cm scale within the sensed depth, which can be used to quantify rock concentration. Generally, elevated RAs can result in significant variations of microwave radiation in terms of T_B through rock's effect on thermal inertia and dielectric permittivity.

When comparing to the “areal abundance” of rocks retrieved from Diviner data (Bandfield et al. 2011, 2017), we use the terms “volumetric abundance” and “MRM RA” interchangeably to express the volumetric fraction of rocks or rock-like materials within the column of each bin. For example, the MRM RA with a value of 0.01 means that 1% volume of lunar regolith is occupied by rocks whose diameters are greater than one-tenth of the wavelength (Ghent et al. 2016). Here, to simplify the soil/rock mixture model, we assume that these materials are mixed homogeneously at all depths, similar to the work of Hu et al. (2018).

The thermophysical properties of rocks are calculated following the work of Bandfield et al. (2011). We used the density of 2940 kg m⁻³, thermal conductivity of 1.491 W m⁻¹ K⁻¹, and a temperature (T) dependent heat capacity (J kg⁻¹ K⁻¹) was adopted from the work of Horai & Simmons (1972), $C(T) = -154.9 + 4.983T - 8.207 \times 10^{-3}T^2 + 5.192 \times 10^{-6}T^3$. Note that the thermal conductivity for rocks is not temperature dependent (Bandfield et al. 2011).

Rocks and soils form a mixture whose thermal properties (TMP) including density, thermal conductivity, and heat capacity, are the volume-weighted average of the rock and soil properties. Here, we neglect the heat diffusion between soils and rocks and calculate the mixture thermal property (TMP_{mix} from volumetric fraction of rocks (V_{rock}) and soil ($1 - V_{\text{rock}}$):

$$\text{TMP}_{\text{mix}} = (1 - V_{\text{rock}}) \times \text{TMP}_{\text{soil}} + V_{\text{rock}} \times \text{TMP}_{\text{rock}}. \quad (1)$$

where TMP_{soil} and TMP_{rock} are thermal property of the soil and the rock, respectively. Here, the regolith density increases with the depth (z), expressed as $\rho(z) = \rho_d - (\rho_d - \rho_s)e^{-z/H}$, where ρ_s is the density at lunar surface, and ρ_d is the density at depths of $z \gg H$ (Vasavada et al. 2012; Hayne et al. 2017). H is a parameter that governs both the regolith density and conductivity and varies spatially (Hayne et al. 2017). As shown in Figure 1(a), H controls density with (dashed lines) and without

(solid lines) 1% rock concentration. However, the mixture thermal conductivity is highly dependent upon the rock concentration and insensitive to H (see Figure 1(b)). Based on the mixture model of thermal property (Equation (1)), Figure 2 shows the modeled temperature profiles of the soil/rock mixture from Figure 1. Note that the surface temperature diurnal variation is constrained by Diviner observations. It can be seen that subsurface temperatures of soils (solid lines) change obviously when mixed with rocks (dashed lines). That is, the rock concentration plays a part in surface/subsurface thermal regime that can be detected by Diviner and the MRM.

Additionally, the elevated RA also suppresses microwave emission from lunar near-surface due to the large permittivity (ϵ) of rocks. Usually the permittivity of substance is represented by relative permittivity $\epsilon_r = \epsilon/\epsilon_0$, where ϵ_0 is vacuum permittivity (8.85×10^{-12} C² N⁻¹ m⁻²). In the case of a two-phase, three-dimensional medium, the dielectric constant of soil/rock mixture (ϵ_{mixed}) is given by Equation (2) (Bergman 1978):

$$(1 - V_{\text{rock}}) \frac{\epsilon_{\text{soil}} - \epsilon_{\text{mixed}}}{\epsilon_{\text{soil}} + 2\epsilon_{\text{mixed}}} + V_{\text{rock}} \frac{\epsilon_{\text{rock}} - \epsilon_{\text{mixed}}}{\epsilon_{\text{rock}} + 2\epsilon_{\text{mixed}}} = 0 \quad (2)$$

where ϵ_{soil} and ϵ_{rock} denote the dielectric constants of soil and rock, respectively. Terrestrial measurements of returned Apollo samples show that ϵ_{soil} is a function of the density, (FeO + TiO₂) content, and radio frequency (Carrier et al. 1991). Recently, a modified dielectric model of lunar soil was proposed by fitting CE-2 T_B data (Siegler et al. 2019), which was employed in this study. Here, we use the Lunar Prospector derived FeO (Lawrence et al. 2002) and LROC WAC derived TiO₂ (Sato et al. 2017) to calculate the dielectric constant of study areas. Additionally, Campbell & Ulrichs (1969) investigated ϵ_{rock} with a wide variety of terrestrial vesicular basalts rocks at 450 MHz and 35 GHz. In this study, the dielectric constant of rock was given as $\epsilon_{\text{rock}} = 5.3 + 0.212i$.

Figure 3 shows the variation of (mixture) permittivity as a function of the depth corresponding to different H parameters and volumetric fraction of rocks. The density-dependent real part (Figure 3(a)) changes only slightly at all H -parameter values when V_{rock} increases from 0 to 0.01. However, the imaginary parts of typical lunar mare (Figures 3(b), (c)) and

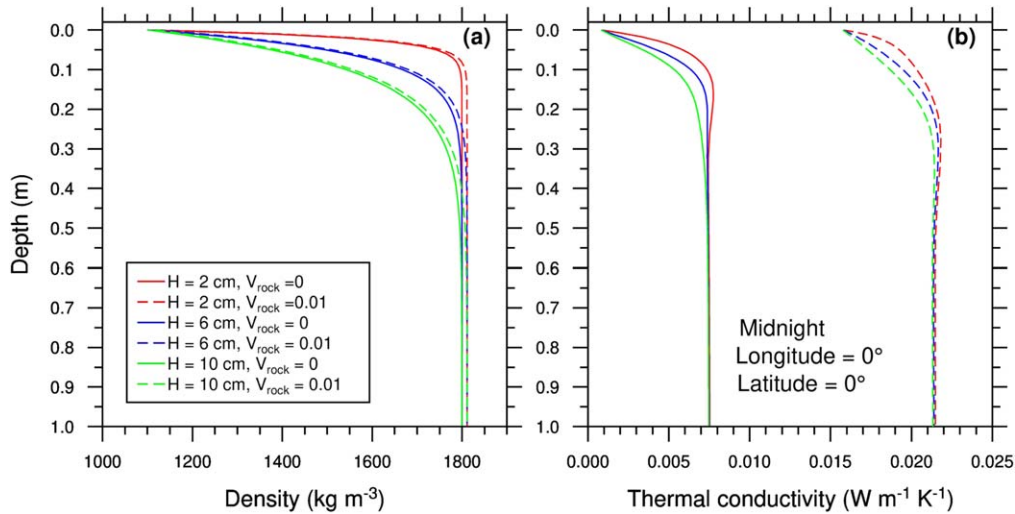


Figure 1. The (a) density and (b) thermal conductivity vary with depth at different values of H parameter and rock concentrations. The thermal conductivity in (b) is calculated at midnight near the center of the lunar nearside.

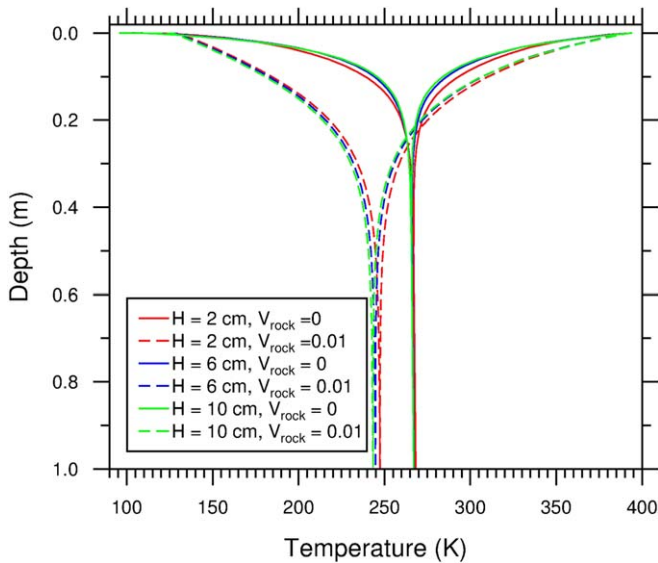


Figure 2. Maximum and minimum temperature profiles as a function of different H parameter and rock concentration (V_{rock}). The solid lines are derived from thermal model without rock; the dashed lines are calculated profiles with $V_{\text{rock}} = 0.01$. The diurnal variation of surface temperatures is constrained by T_{Bol} .

highland (Figures 3(d), (e)) at the two MRM channels are more sensitive to the increase of rock concentration.

In order to demonstrate how the RA influence microwave emissions, here we show an example of modeled microwave brightness temperatures for the soil and the soil/rock mixture (Figure 4). Note that both $T_{\text{B}7}$ and $T_{\text{B}19}$ are simulated based on temperature profiles of Figure 2 and the mixture dielectric constant of Figures 3(a), (d), and (e) (typically highland). Obviously, the elevated RA affects T_{B} diurnal variations, especial for the nighttime. Therefore, the enhanced rock “signal” can be detected most readily in the nighttime by the MRM channels, which, in turn, is used to retrieve RA from MRM observations.

Here, it is worth noting that the spatial resolution of 3 GHz observations (25 km) is larger than that of 7.8, 19.35, and 37 GHz (17.5 km). This will cause additional T_{B} differences between 3 GHz and the other channels especial for the

horizontally inhomogeneous rocky areas where we focused on in this study. To avoid retrieval uncertainties of RA, the $T_{\text{B}3}$ data are not used here, though it can sense greater depth. To retrieve RA, we initially considered two data groups (7.8 and 19.35 GHz) and (19.35 and 37 GHz) in our rock model. However, we found that the retrieved RA values were not stable from the latter data group. Whereas the former data group was used in this study because of the stable results by comparing with Diviner RA and radar observations. Recently, several researchers (e.g., Hu et al. 2017; Feng et al. 2020) suggest that there are calibration issues at lower frequencies (3 and 7.8 GHz) which might be attributed to heat contaminations. Feng et al. (2020) proposed an offset of 18 K to recalibrate 7.8 GHz data by eliminating typical rocky areas that have more than 1% Diviner RA. We employed this offset value to recalibrate 7.8 GHz data and retrieved RA, however, the result showed that the RA value is randomly distributed by comparing with non-recalibrated data and Diviner RA. More discussions of calibration uncertainties of 7.8 GHz data will be presented in Section 4.1.

In this study, we inverted the volumetric RA based on the differences of thermal property and permittivity between the soil and the rock. The models of thermal and T_{B} were combined in our rock model that uses the Diviner data as surface thermal constraint. The detailed processes are described in the following steps:

- (1) computing the density, thermal conductivity and specific heat capacity of the soil/rock mixture from Equation (1). We adopt Hayne et al.’s (2017) method to calculate thermal property of lunar soil. And the rock’s thermal parameters are given based on the work of Horai & Simmons (1972) and Bandfield et al. (2011).
- (2) setting up the soil/rock mixture thermal model using T_{Bol} as surface thermal constraint following the work of Wei et al. (2019). Thus, we can derive subsurface temperatures at each bin.
- (3) calculating the mixture dielectric constant. ϵ_{soil} was calculated based on Siegler et al. (2019) and ϵ_{rock} was assumed as a constant which is independent of frequency and temperature (Campbell & Ulrichs 1969). ϵ_{mix} was

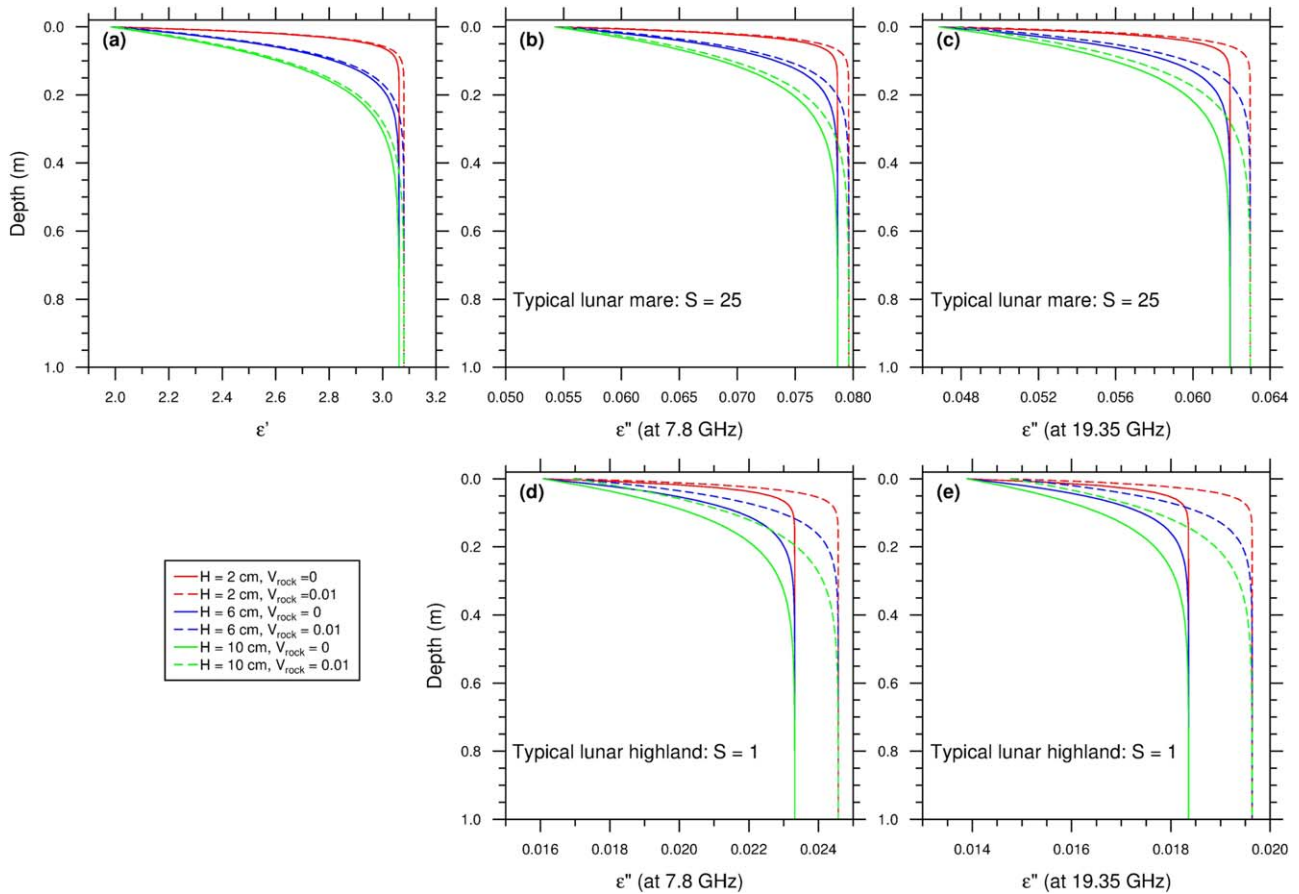


Figure 3. Permittivity vs. depth at different rock concentration and H parameter. (a) is the real part of permittivity at different H parameter and rock concentrations. (b)/(c) and (d)/(e) are variations of imaginary parts vs. depth at 7.8 and 19.35 GHz, respectively, for typical lunar mare and highland. Note that S stands for the $(\text{FeO} + \text{TiO}_2)$ content in weight percentage.

derived based on two-phase dielectric constant model of Equation (2).

- (4) modeling the mixture T_B and retrieving V_{rock} . Based on the derived subsurface temperatures and ε_{mix} from the above steps, the MRM's nighttime observations (T_B^O) are fitted by simulated microwave brightness temperature (T_B^S) with two parameters, (1) volumetric rock fraction (0%–100%) and the (2) H parameter (0–10 cm). Therefore, the V_{rock} and H parameter can be obtained by minimizing the differences between T_B^O and T_B^S as

$$V_{\text{rock}}, H = \arg \min [(T_{B7}^O - T_{B7}^S)^2 + (T_{B19}^O - T_{B19}^S)^2]. \quad (3)$$

3. Results

The global Diviner observations show that most lunar surfaces are relatively free of rocks, but elevated rock concentrations are associated with small craters (>100 s of meters in diameter) and large young impact craters (Bandfield et al. 2011). Although most of these small craters cannot be resolved at the resolution of the MRM, the concentrated rocks contribute to the overall microwave emission within its field of view. As a result, this can also lead to different values of rock concentration at each bin. Notably, although two measurements and two unknowns are presented in the model, we found that the solution of the H parameter is not convergent at study areas. It is assumed that the MRM observations are more sensitive to

RA variations than that of the H parameter. That is, the minimized rms value is much dependent upon the rock concentration. In this section, we report the optimized values of RA at several typical craters and highlands to characterize the surface morphology and geological evolution of the Moon.

3.1. Rocky Craters

Large rocky craters can be characterized by our retrieved rock concentrations. Here, we report on the well-preserved Copernican impact crater Aristarchus, which is 42 km in diameter and lies on the southeastern edge of the Aristarchus Plateau, one of the most geological interesting regions on the Moon (McEwen et al. 1994). The Aristarchus Plateau, covered by a mixture of basalt flows and fine-grained pyroclastics (Campbell et al. 2008), is a raised rectangular (170×200 km) ancient highland crust that is ~ 2 km above the surrounding basaltic plains. The dark, reddish pyroclastic glass revealed by Clementine multispectral observations covers the plateau to average depths of 10–30 m (McEwen et al. 1994).

As shown in Figure 5(a), there is a dramatic contrast in RA between the Aristarchus crater (enclosed by white box) and the plateau. Nevertheless, it still shows a relatively high rock concentration around the edge of the plateau and Vallis Schröteri, located near the plateau's center. Within the Aristarchus crater, RA decreases from the northeast to the southwest. Exposed rocks retrieved from Diviner observations

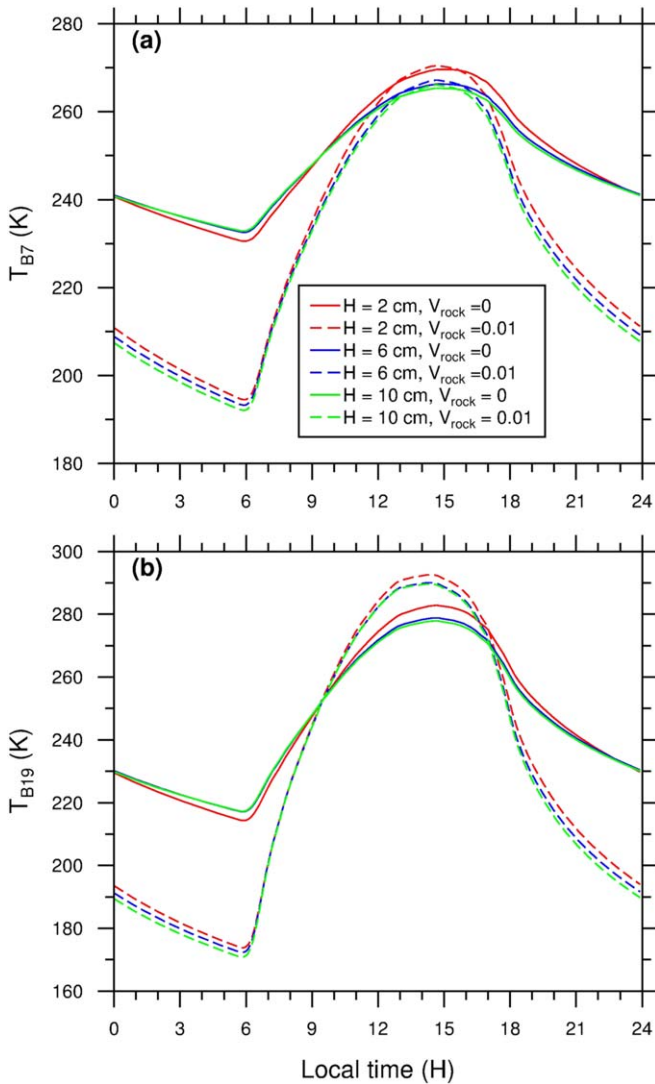


Figure 4. The effect of rock concentration on diurnal variations of (a) T_{B7} and (b) T_{B19} at the center of the lunar nearside. The content of (FeO + TiO₂) is given as 1 (in percentages) here.

(Bandfield et al. 2011; Figure 5(b)) have a similar distribution to our results.

To characterize the morphology of Aristarchus crater with the combination of MRM and Diviner rock concentration, we define the “rock thickness,” d_{rock} . That is, the volumetric MRM RA (RA_{MRM}) is divided by areal Diviner RA (RA_{Diviner}), i.e., $d_{\text{rock}} = RA_{\text{MRM}}/RA_{\text{Diviner}}$, where the value of d_{rock} represents the equivalent rock thickness in percentages of the microwave penetration depth. For example, $d_{\text{rock}} = 0.1$ indicates that the “thickness” equals to 10% of the 7.8 GHz channel’s penetration depth. A larger value of d_{rock} indicates (1) more rocks and/or fragments are buried in the subsurface, and/or (2) more small surface rocks that have not been sensed by the Diviner RA model. Therefore, d_{rock} provides us with a basic geology index and implication for rocks and rock-like materials. Figure 6 shows the distribution of equivalent “rock thickness” at the Aristarchus crater; it also presents a decreasing trend from the northeast (0.2) to the southwest (0.08) of the crater, which suggests a larger number of near-surface rocks concentrated northeast of the crater.

To better understand the rock concentration characterized by the “rock thickness,” we selected two regions of interest (ROIs) with the size of $0^{\circ}25 \times 0^{\circ}25$ that both cover crater rims and walls (see boxes A and B in Figure 6). Figures 7 and 8 show a remarkable contrast in rock concentrations and distributions, though both of the NAC images contain obvious impact melts and lava flows. For the area with a large value of d_{rock} (box A in Figure 6), there are ubiquitous rocks in the study area, where most of them are mantled by impact melts (see the right panels of Figure 7). This results in increased values of d_{rock} due to large amounts of buried rocks that might not be sensed effectively by the Diviner RA model due to the formation of regolith and maturation in the past millions of years. In addition, enhanced radar echoes and the presence of numerous radar-bright regions also confirm that this mantle is heavily contaminated by rocky materials (Campbell et al. 2008). In contrast, the area with a small d_{rock} value (Figure 8) shows fewer rocks that tend to concentrate and are partially buried within the study area (see right panels of Figure 8).

3.2. Hummocky Regions

In addition to the exposed rocks, there are also a large number of blocks and fragments that were displaced and deposited during the impact event (Sturm et al. 2015; Krüger et al. 2016). The melt deposits, including a mixture of melt and clastic debris, create the typical hummocky terrain (Bray et al. 2010) that is prominent at fresh craters. For example, the young Tycho crater (85 km in diameter) shows a large chaotic landscape on the crater floor and typical melt pools and flows all along the terraced walls (Krüger et al. 2016). The central peaks of Tycho crater also display notable impact melts and signs of mass wasting. Figure 9(a) exhibits an extensively elevated RA that covers the central peaks, floor, and walls. It also presents a similar distribution range with exposed rocks (Figure 9(b)). However, the MRM RA shows a relatively homogeneous distribution for the near-surface of the crater floor, while there are more surface rocks on the eastern floor and walls.

Recent work on the morphology of the floor of the Tycho crater shows it exhibits a distinguishable hummocky texture and boulder concentration (Krüger et al. 2016; Dhingra et al. 2017). Based on Kaguya Terrain Camera and LROC data, Krüger et al. (2016) produced a high-resolution geomorphological and impact melt distribution map for Tycho crater. They characterized the floor by three morphological units: (1) the high hummocky unit covering the western part of the floor, (2) the low hummocky unit covering the northern and southern parts of the floor, and (3) the smooth unit covering the eastern part. This also agrees well with the distribution of surface roughness (Dhingra et al. 2017). As shown in Figure 9, we delineated the whole area (enclosed by white lines) of high/low hummocky units of the crater floor and central peaks following the work of Krüger et al. (2016). As expected, the distribution of MRM RA on the floor correlates better with the hummocky units than that of Diviner RA. That is, a large number of melt deposits including blocks, rocks, and fragments within this area are effectively detected by the MRM rock model. In contrast, the smooth and non-hummocky area (the area outside the white line) associated with enhanced MRM RA is expected to be mainly caused by exposed and/or partial buried rocks as revealed by Diviner RA. The discrepancy between MRM RA and Diviner RA indicates geological processes that include

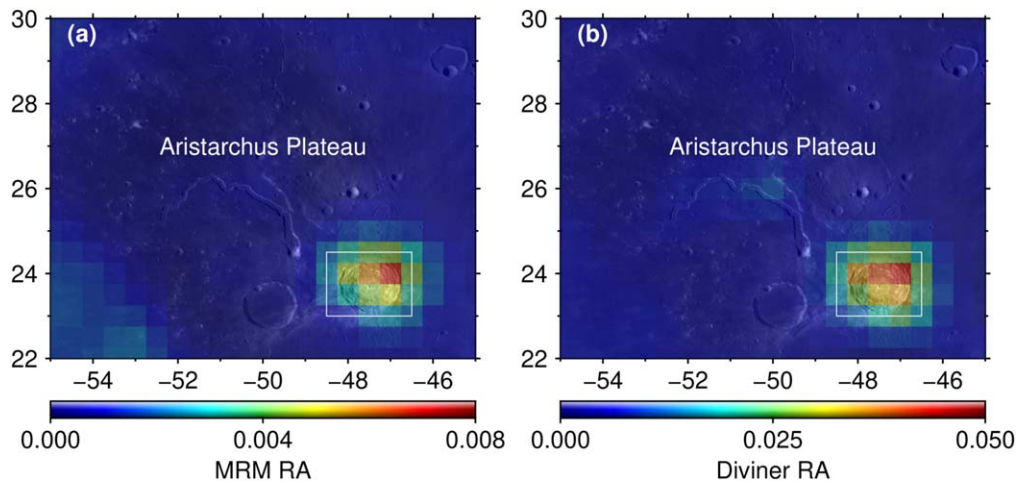


Figure 5. Rock abundances at the Aristarchus plateau and crater retrieved from (a) MRM and (b) Diviner measurements, respectively. The WAC images are used for mosaics. The Aristarchus crater is enclosed by the white box, which will be investigated in detail below.

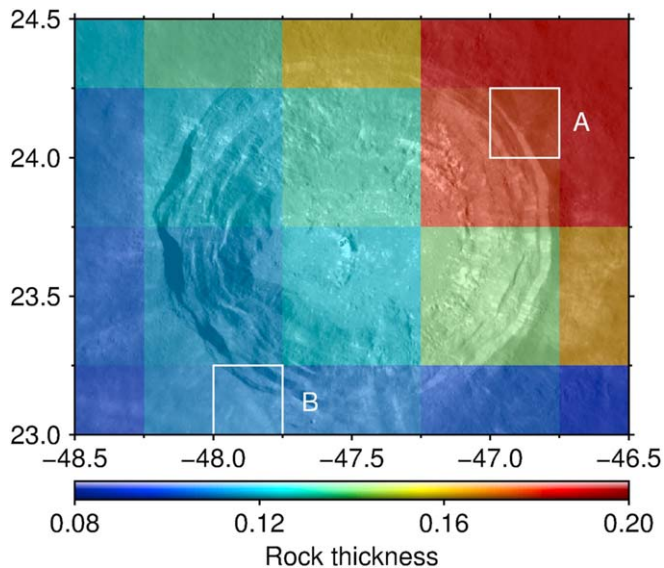


Figure 6. Distribution of equivalent “rock thickness” at the Aristarchus crater. The WAC image is used as a mosaic. The white boxes labeled by A and B are ROIs that will be investigated by NAC images in Figures 7 and 8, respectively.

melt flow, rock displacement, and rock deposition as a result of the W-SW impact cratering (Dundas & McEwen 2007; Krüger et al. 2016). Dhingra et al. (2017) also mapped 15 geological units on the crater floor. Their mapped hummocky texture and blocks are in good agreement with our MRM RA distribution.

3.3. Impact Melts at Highlands

Large areas of impact melts associated with elevated RA have also been identified in the highlands. One example is the Tycho antipode region, which is thought to have been formed by ballistically emplaced impact melts during the Tycho crater impact (Robinson et al. 2011). This region exhibits terrain with unique geomorphology and physical characteristics that show a distinct and extensive rock concentration and melt features (Bandfield et al. 2017; Paige et al. 2018). As shown in Figure 10(a), elevated rock concentrations are present as a large patch centered near 167°5 E, 42°5 N. The extent of this elevated rock concentration is similar to that of impact melts (enclosed by the white line)

identified from NAC images (Robinson et al. 2016). In contrast, the exposed rocks observed from Diviner RA data (Figure 10(b)) tend to be concentrated in the southern part of the melt-deposit area.

Based on NAC observations, Figure 11 shows a large number of small melt ponds with flat, uniform albedo deposits of different thickness (Robinson et al. 2016) that are distributed around crater rims (indicated by white arrows). The melt deposits on the floors of craters, depressions, and smooth plains are comprised of a mixture of melt and solid rock fragments that have been incorporated during melt movement and emplacement (Bray et al. 2010). These buried rocks and/or debris have been shielded by the solidified melts and flows, but they can be penetrated by microwave waves. In addition, cracks with rubble piles, which occur as polygonal and irregular patterns (indicated by yellow arrows) are prominent on the pond surfaces. The variation of morphology—for example, cooled melt breccia and deposits and solid fragments among the three ROIs (Figures 11(A)–(C))—agrees well with the variation of MRM RA.

3.4. Validation by Comparing Radar Observations

In reality, the size and burial depth of rocks (parameters that are not taken into account in our rock model) also cause uncertainties in the interpretation of CE-2 microwave observations. Although the LROC provides us with high-resolution images to characterize the morphology of the lunar surface, we are still unable to quantify the MRM RA by comparing NAC images directly for several reasons. They are (1) a large number of small rocks (<0.5 m, the threshold of NAC resolution) that cannot be identified by NAC images, (2) some rocks are buried in the subsurface, and (3) random shapes of exposed and/or partially buried rocks make volume estimation inaccurate. Nevertheless, the general agreement of rock distribution retrieved from MRM and Diviner measurements as described above at the Aristarchus crater, the Tycho crater, and the Tycho antipode indicates the reliability of our retrieval results. In addition, good agreement between rock concentration and morphological units identified by Robinson et al. (2016), Krüger et al. (2016), and Dhingra et al. (2017) also provides a qualitative validation of our inversion results.

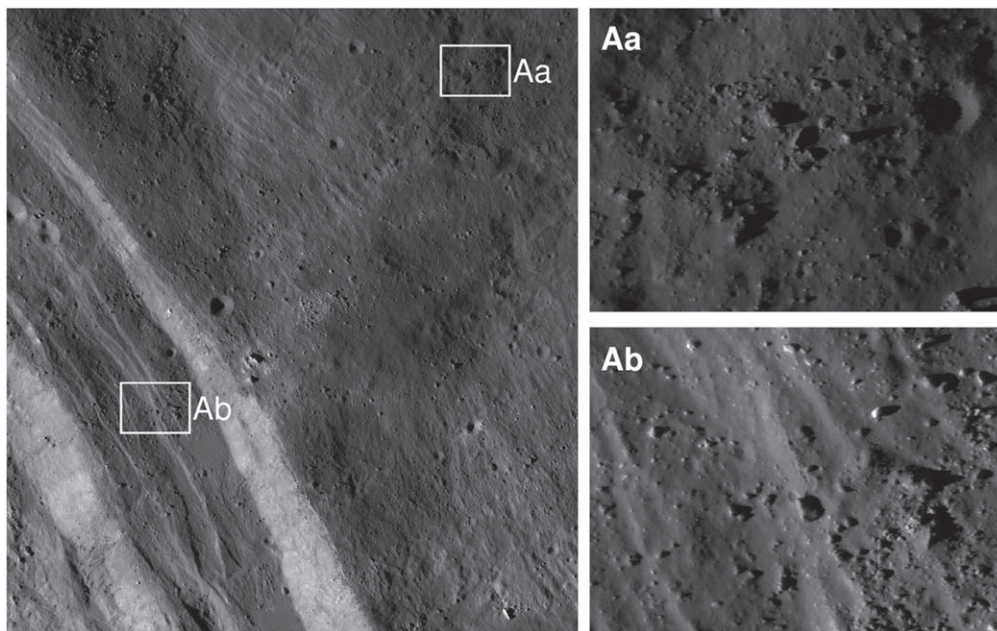


Figure 7. NAC images of the ROI (box A in Figure 4) at the Aristarchus crater. Both the width of panels (a) and (b) are 830 m.

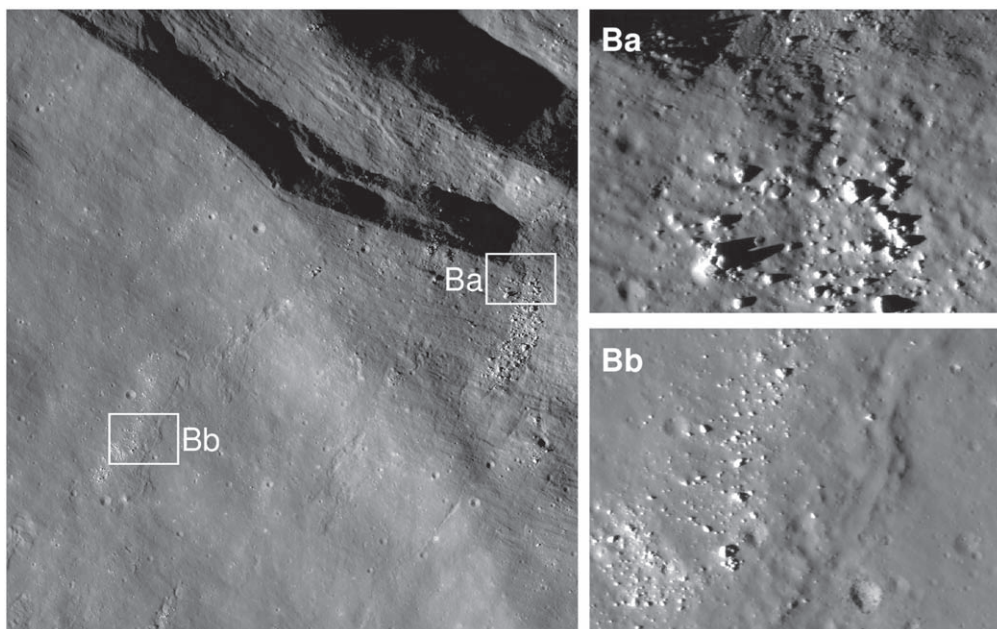


Figure 8. NAC images of the ROI (box B in Figure 4) at the Aristarchus crater. The width of both panels (a) and (b) are 837 m.

Radar observations are highly sensitive to both surface and buried rocks that have similar sizes to the wavelength of measurement. Therefore, radar measurements have the ability to probe the subsurface and glean information about buried rocks (Bandfield et al. 2011; Ghent et al. 2016). For example, the LRO's Miniature Radio Frequency (Mini-RF) *S* band (~ 12.6 cm wavelength) is sensitive to the presence of rocks and heterogeneous materials in the upper ~ 1 – 2 m of regolith (Nozette et al. 2010; Carter et al. 2012; Neish et al. 2013; Cahill et al. 2014). This allows for the detection of melt flows, pond features, and shallowly buried rocks (Bandfield et al. 2017). Usually, the circular polarization ratio (CPR) is used to investigate subsurface scatters (such as rocks) in addition to surface roughness, which have the same size as the wavelength

of the signal (Campbell et al. 2010). CPR is defined as a dimensionless parameter, which is the ratio of return signals between the same sense circular polarization as transmitted and the opposite sense circular polarization (Bandfield et al. 2017).

Figure 12(a) presents a prominent distribution of rock concentration at the Tsiolkovskiy crater. Notably, there is a large extent of elevated rock concentration at the southern and southeastern rims and ejecta. Tsiolkovskiy (180 km diameter) is partially filled by mare basalt and is associated with distinct impact melts and ejecta deposits (Greenhagen et al. 2016). The location of the enhanced rock concentration to the southeast of the crater is generally coincident with an impact melt deposit first identified in images by Hawke & Head (1977). The enhancement of RA in the melt deposit can be explained by the

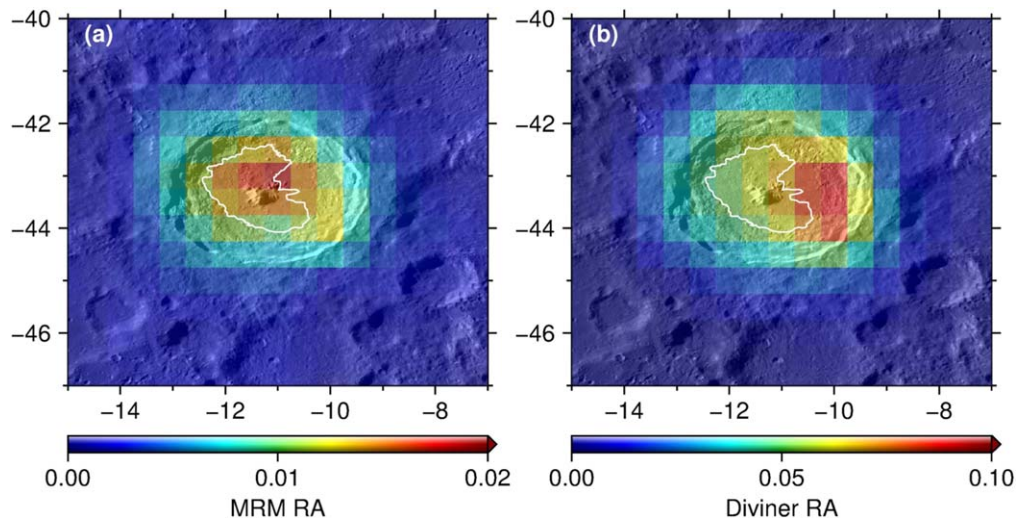


Figure 9. Distribution of (a) MRM RA and (b) Diviner RA at the Tycho crater. The area enclosed by the white line includes the high/low hummocky region and central peaks, which is delineated from the work of Krüger et al. (2016).

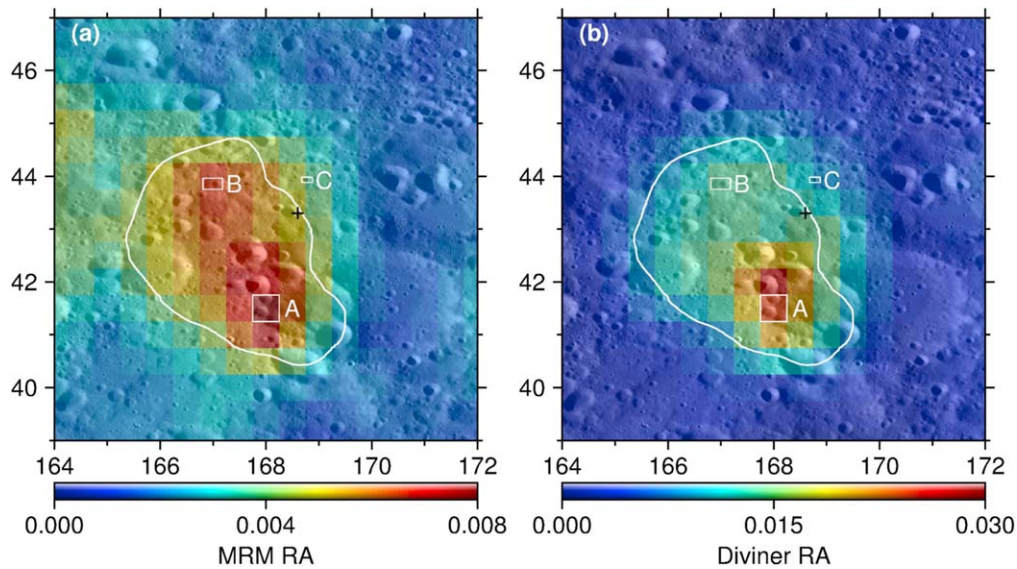


Figure 10. Distribution of (a) MRM RA and (b) Diviner RA at the Tycho antipode region. The area enclosed by the white line shows the widespread thin and discontinuous veneer of material, delineated from the work of Robinson et al. (2016). The black cross denotes the exact antipode point of the Tycho crater. The white boxes labeled by A, B, and C are ROIs shown in Figure 11.

rocky ejecta that are excavated by small impact craters in the massive coherent melt sheet. As shown in Figure 12(c), the high CPR values in the southeastern and northeastern portions of the Tsiolkovskiy crater suggest the presence of massive melt deposits and/or exposed rocks. For example, study regions A and B in Figure 12 present numerous, partially buried small rocks (as seen Figure 13) that agree well with enhanced MRM RA and CPR values. In addition, the MRM RA also shows a similar distribution to the exposed rocks (Figure 12(b)), especially for the extended south and near-east ejecta. This large and interesting asymmetric distribution of rocks might be attributed to a high-velocity impact event that produced more melts at Tsiolkovskiy than the typical Late Imbrium-age craters (Greenhagen et al. 2013; Neish et al. 2013).

4. Discussion

4.1. Calibration Uncertainties of 7.8 GHz Data

Recently, several works (Hu et al. 2017; Feng et al. 2020) suggested that there are calibration uncertainties of CE-2 MRM's low-frequency data (i.e., 3 and 7.8 GHz). This is most likely caused by heat contamination of the second set of space-looking calibration horns from comparison with theoretical simulations (Hu et al. 2017). Feng et al. (2020) proposed an offset of 18 K to calibrate the 7.8 GHz channel data using Diviner channel 7 data as the surface thermal constraint. It is worth noting that the offset value was derived in their work by eliminating high rocky areas based on Diviner RA values. Nevertheless, since the T_{B7} data encountered a global

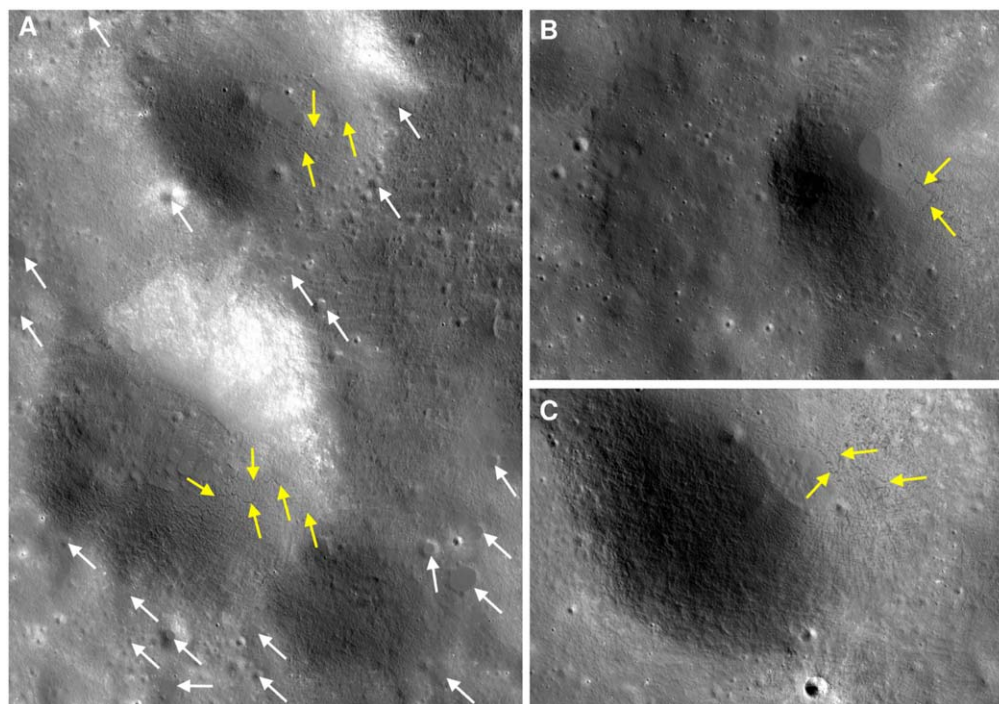


Figure 11. NAC images at the Tycho antipode region. Image widths of (A), (B), and (C) are 11.36 km, 8.11 km, and 4.37 km, respectively. White arrows indicate the small ponded melts. Yellow arrows indicate cracks with rubble piles that formed at the intersection between flows (Robinson et al. 2016). See Figure 10 for locations.

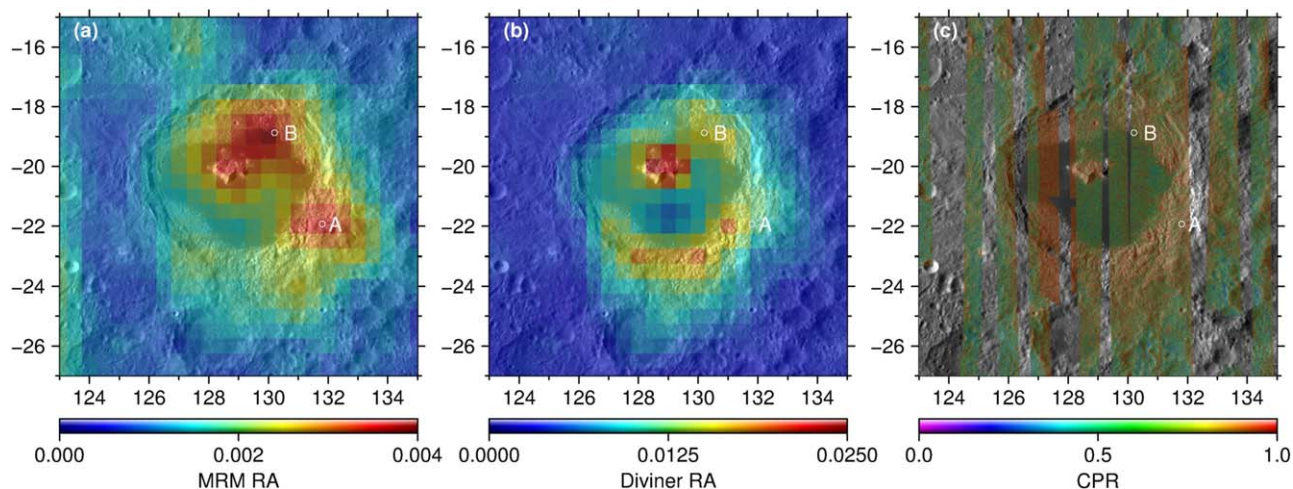


Figure 12. Comparison of rock concentrations at the Tsiolkovskiy crater retrieved from (a) MRM, (b) Diviner observations, and (c) their corresponding CPR values derived from Mini-RF. The WAC image is used for mosaic. The white circles labeled A and B are ROIs that were shown in Figure 13. Note that the CPR image data is derived based on JMARS software.

calibration issue, the rocky areas can also encounter a similar calibration uncertainty as well as rock-free areas.

Assuming the same offset (18 K) at rocky areas, we adjusted the observed T_{B7} data (i.e., $T_{B7}^O + 18$) and inverted the MRM RA at the Aristarchus Plateau, for example (Figure 14). We can see that the calibrated T_{B7} derived RA (Figure 14(a)) shows a similar value range with original T_{B7} retrieved RA (Figure 14(b)). But the former presents the highest MRM RA values near the southwest of the Plateau but lower values at the Aristarchus crater. It seems that the MRM RA values at the Aristarchus crater was suppressed but the southwest area was raised after adjusting the T_{B7} with an offset of 18 K. This plausible over/under estimated scenario is different with original T_{B7} derived RA and Diviner RA that

were supposed to be more reliable in the plateau area. We suppose that the simple calibration—for example, adding the offset 18 K here—might add an additional “artificial” T_B in our rock inversion model. In fact, each bin of the study area (e.g., the Aristarchus Plateau) should be calibrated by adding different offset values because of the complexity thermo-physical property of soil/rock mixture. Instead, using the original T_{B7} data can avoid the additional “artificial” T_B that results in reliable MRM RA values across this area by comparing with Diviner RA. However, to better constrain the volumetric fraction of rocks, a more accurate calibration scheme of T_{B7} is necessary in the future work.

We also tried to use the high frequency data sets (i.e., 37 and 19.35 GHz) instead of 19.35 and 7.8 GHz group data to invert

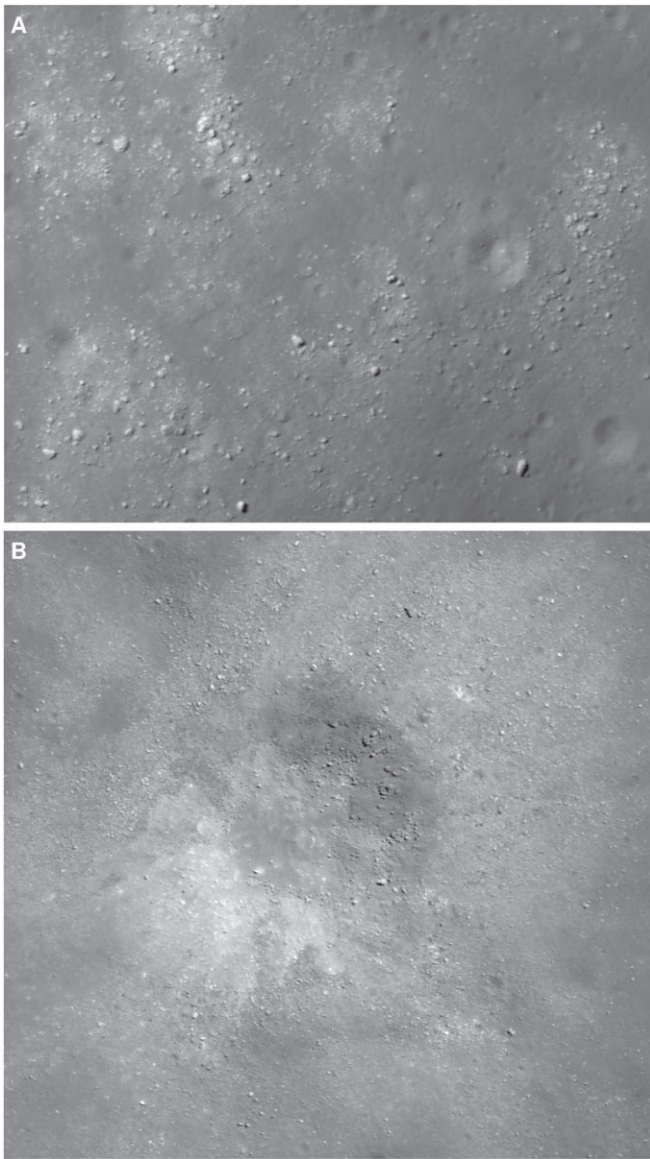


Figure 13. NAC images of ROIs at the Tsiolkovskiy crater. Panel (A) is from the NAC frame M1235740523LC. The width is 703 m with the center at 132°16 E, 21°99S and the resolution of 1.5 m pixel⁻¹. Panel (B) is from the NAC frame M126079244LC. The width is 658 m with the center at 130°21 E, 18°87S and the resolution of 0.60 m pixel⁻¹. The locations of panels (A) and (B) are also labeled in Figure 12.

MRM RA because of their less calibration issue. However, we find that the inverted MRM RA values are randomly distributed in the study area without any geological features comparing to that of 19.35 and 7.8 GHz group data and Diviner RA. We suppose that it might be caused by topographic effect (very close to surface temperatures for the 37 GHz at rocky areas) and microwave scattering of fragments at sub-centimeter scale (the wavelength of 37 GHz is ~ 0.81 cm). In fact, the EM scattering is influenced by a multitude of parameters of the target, such as shape, dielectric property and orientation (Woodhouse 2007). In our rock model, we neglect the scattering effect (Rayleigh and Mie scattering). That is, the rocks with the size less than one-tenth of wavelength at 7.8 GHz (~ 3.8 cm) will not be included in MRM RA. Nevertheless, this did not influence our inversion results and geological interpretation by comparing with Diviner RA. In the

future work, an improved rock model considering the scattering effect will reveal more details of rock concentration and geological interpretations.

4.2. Influence of Spatial Resolution on MRM RA

The high resolution of remote sensing data like Diviner observations and NAC images can detect more detailed geological features such as small rocky craters. Due to the large coverage of CE-2 MRM's field of view and randomly distributed rocks on the lunar surface, the retrieved MRM RA value at each pixel can only represent a homogeneously distributed rocky area. That is, small rocky craters (much less than 17.5 km in diameter) within the bin, for example, cannot be characterized in terms of elevated MRM RA values. However, the retrieved MRM RA at each bin still provide a "perspective" view of volumetric fraction of rocks for large impact craters that reworked lunar surface in the past billions of years. Because the CE-2 is the copy of CE-1, the MRM data were obtained during their separated missions (Zheng et al. 2012, 2019). The lower orbital altitude of CE-2 (only one half of CE-1's) improved the MRM spatial resolution by a factor of 2. In addition, the "microwave cold spots" (Zheng et al. 2012; Zhu et al. 2019) and "low- T_B spots" (Chan et al. 2010; Zheng et al. 2019) have been identified by both CE-1 and CE-2 observations. These thermal anomalies are interpreted as rock influences (Zheng et al. 2019). Here, we present a direct T_B comparison at rocky craters between CE-1 and CE-2 to investigate the rock-induced thermal anomalies under different spatial resolutions.

Figure 15(a) shows the coverage of CE-1 nighttime (00:00–06:00) T_{B19} at the Tycho crater. Although it shows an apparent latitude effect, the T_{B19} decreases within the crater, which is attributed to near-surface rocks as shown in Figure 9. For the same local time range, the CE-2 T_{B19} (Figure 15(b)) presents a prominent thermal anomaly within the crater. It suggests that an enhanced "signal" corresponding to a large number of RAs is detected within a smaller field of view (i.e., higher spatial resolution). Therefore, more geological features, including rocks, can be characterized by higher spatial resolutions of microwave observations. In this study, for the limit of CE-2's MRM resolution, we were only able to retrieve a low spatial resolution of MRM RA for large areas. This also illustrates that the change in response with spatial resolution can also present critical geological information about near-surface rock concentration, adding to the Diviner data-derived surface rocks.

4.3. Nighttime Low- T_B of Rocky Craters

Both CE-1 and -2 MRM measurements have revealed T_B anomalies globally (Chan et al. 2010; Zheng et al. 2012, 2019; Zhu et al. 2019), but these have not been discussed in detail in terms of rock concentration. Low- T_B features in the nighttime can be characterized by data obtained at different microwave frequencies (or wavelengths). Here, we present a series of low- T_{B7} and low- T_{B19} maps at a typical rocky crater at different times during the night. We then correlate the T_B values with rock concentrations to illustrate rock-dependent, near-surface thermal behavior.

Figure 16 shows the time dependence of T_{B7} (upper row) and T_{B19} (lower row) at the Jackson crater. At first glance, the crater presented apparently low- T_B features in both channels through the night. Notably, however, T_{B7} is higher than T_{B19} at these

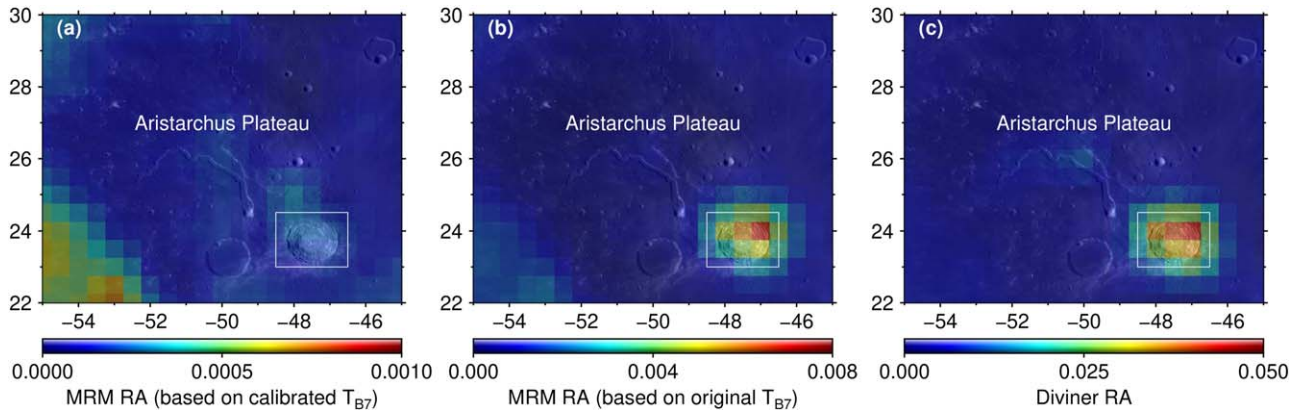


Figure 14. Comparison of RA at the Aristarchus Plateau. (a) The derived MRM RA based on recalibrated T_{B7} (Feng et al. 2020). (b) The derived MRM RA with original T_{B7} used in this study. (c) The Diviner RA (Bandfield et al. 2011) that are reduced to the same resolution with MRM RA. The white box indicates the Aristarchus crater. Note that both (b) and (c) are the same with Figure 5.

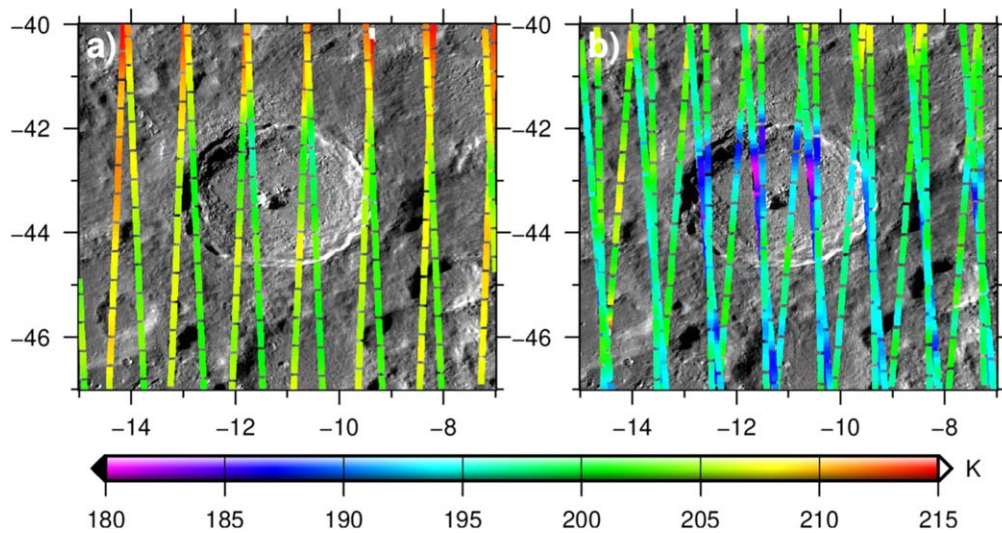


Figure 15. Comparison of nighttime (00:00–06:00) T_{B19} covering at the Tycho crater between (a) CE-1 and (b) CE-2 observations.

local times. This is because the warmer subsurface can be sensed by the longer wavelength signals. The two channels' low- T_B suggests a wide range of geological units that are influenced by high permittivity materials such as rocks and ilmenite.

As shown in Figure 17(a), the retrieved RA shows an extensive and nearly symmetric distribution. Specifically, the rock concentration decreases gradually from central peaks to the walls and ejecta. This agrees well with the distribution of low- T_B regions that are measured by 7.8 and 19.35 GHz channels at different times during the night. In contrast, Figure 17(b) presents a relatively lower content of (FeO + TiO₂) at the Jackson crater than the surroundings, which would result in a relatively higher T_B due to less microwave suppression. These two contrary effects resulted in low- T_B features at the crater, indicating that the elevated rock concentration is the main influence on T_B . It also suggests that the effect of (FeO + TiO₂) on T_B has been removed effectively in our model.

To quantify the correlation between MRM observations and rock concentration, we plot T_B versus RA from all data points of the region at different local times. Figure 18 shows that both T_{B7} and T_{B19} decrease with increasing rock concentration. T_{B19} (Figure 18(b)) decreases ~ 10.1 K, with RA increasing from

0.0015 to 0.0088 at the local time range 1900–2100 (red dots). T_{B19} decreases ~ 17.3 K with similar RA increasing at the time range 0300–0500 (blue triangles). Figure 18 shows that microwave brightness temperature and its nighttime cooling rate is dominated by rock concentration.

4.4. Degradation of Rocky Craters

It is interesting to correlate the rock concentration with crater age to help us understand the degradation of craters and the evolution of lunar regolith. The Diviner RA has been cautiously correlated with crater ages because the coverage of impact melts and mass wasting can mask abundant rocks (Bandfield et al. 2011; Ghent et al. 2014). Hence, inaccurately estimating rock concentrations could cause uncertainties for quantifying the degradation of craters and the evolution of lunar soils.

We correlate the MRM RA of seven large craters with published model ages derived from crater size–frequency distribution measurements. Figure 19 (left two columns) shows the distribution of MRM rock concentration at different craters. Here, the model ages of the Necho, Tycho, Jackson, Aristarchus, and Copernicus craters are given based on the

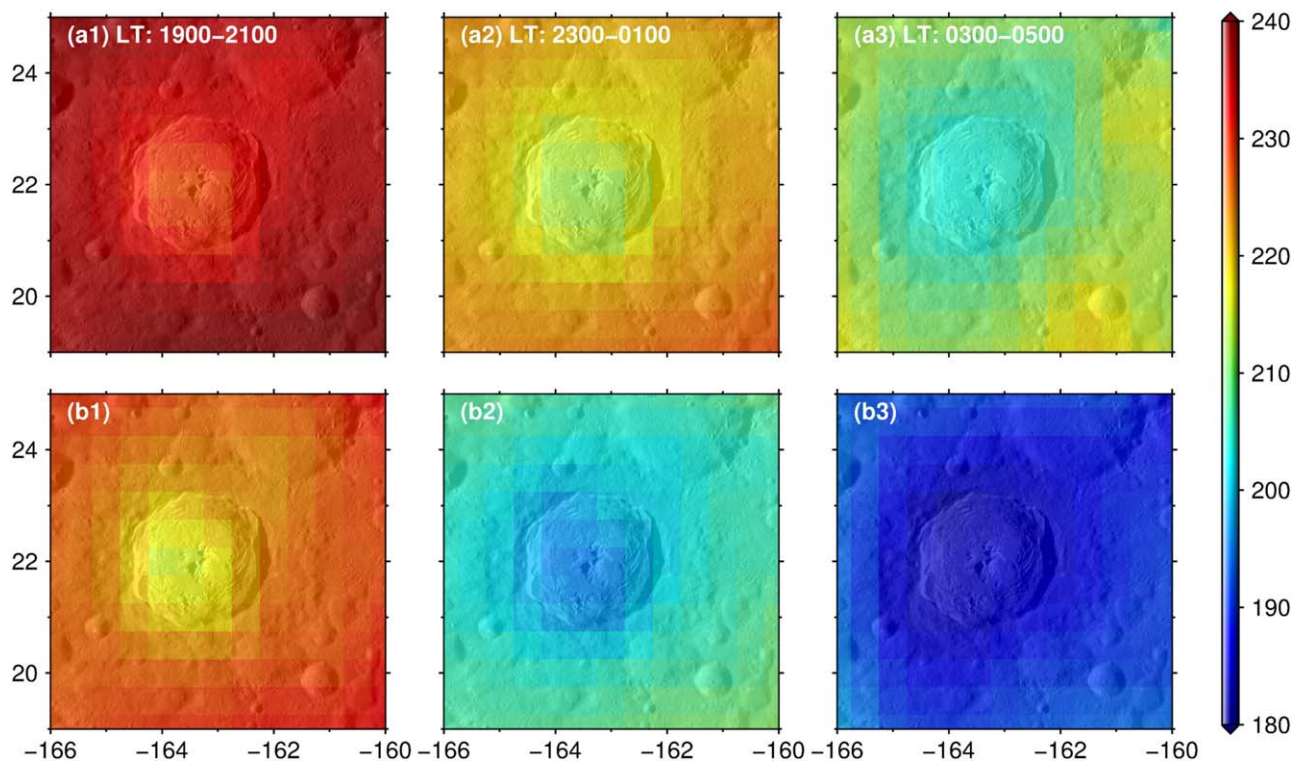


Figure 16. Distribution of T_{B7} (upper row) and T_{B19} (lower row) at the Jackson crater at night. a1/b1, a2/b2, and a3/b3 correspond to the local times (LT) 1900–2100, 2300–0100, and 0300–0500, respectively. The WAC images are used for mosaics.

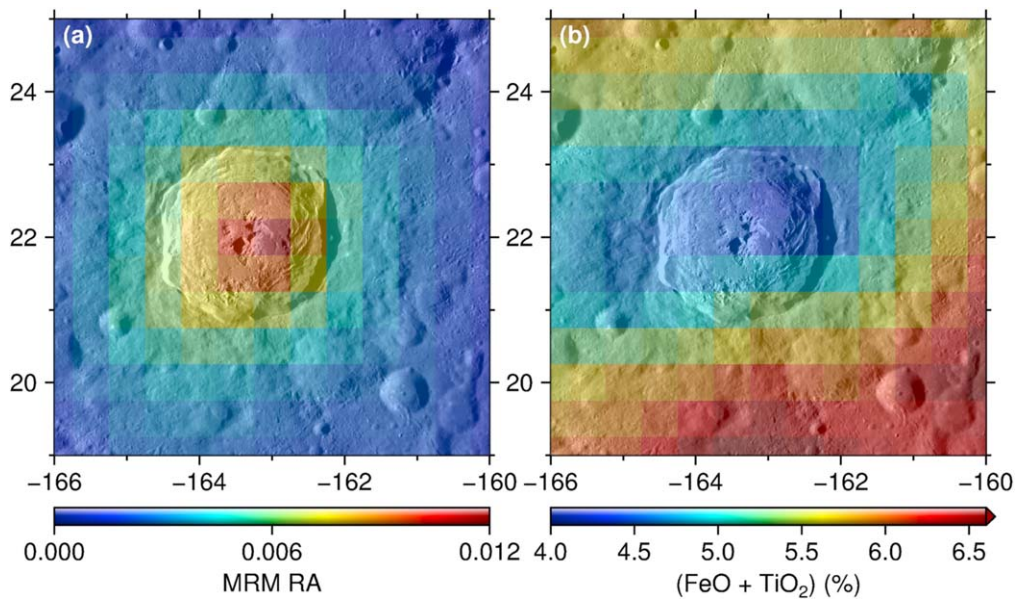


Figure 17. Distribution of (a) rock concentration and (b) $(\text{FeO} + \text{TiO}_2)$ at the Jackson crater. The WAC image is used as mosaic.

work of Ghent et al. (2014). The Tsiolkovskiy crater age is given by Greenhagen et al. (2016), and the Humboldt crater age is given by Martinot et al. (2018). Generally, the elevated rock concentrations within craters present a decreasing trend with increasing ages. It can also be deduced that the relatively high rock concentrations within craters are associated with prominent impact melts. It is assumed that the impact melts in the crater are coherent flows from melt deposits that likely degrade more slowly than the surrounding ejecta blankets (Neish et al. 2013). The younger craters (e.g., Necho and Tycho) are dominated by high concentrations of rocks that

break down within a short geological time (Thompson et al. 1974; Mendell 1976; Bandfield et al. 2011).

It is also interesting to compare surface rock concentration retrieved from Diviner measurements (Bandfield et al. 2011). Figure 19 (right two columns) shows that the surface rock concentration presents a similar decreasing trend with MRM RA (left two columns) from young to old craters. It suggests that rocks exposed on the surface and/or buried in the soil will be broken down and form the soil in the past billions of years. The differences of rock distribution and breakdown rate between MRM RA and Diviner RA among these craters

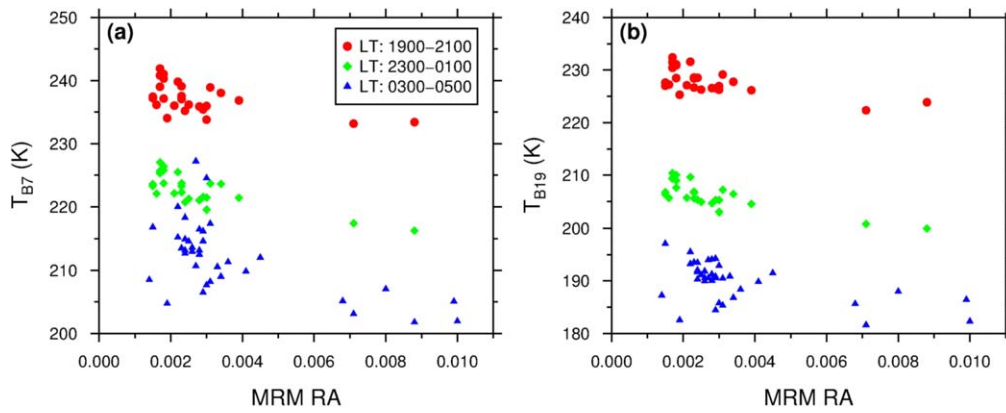


Figure 18. The CE-2 observed (a) T_{B7} and (b) T_{B19} vs. rock concentration at different local times at the Jackson crater.

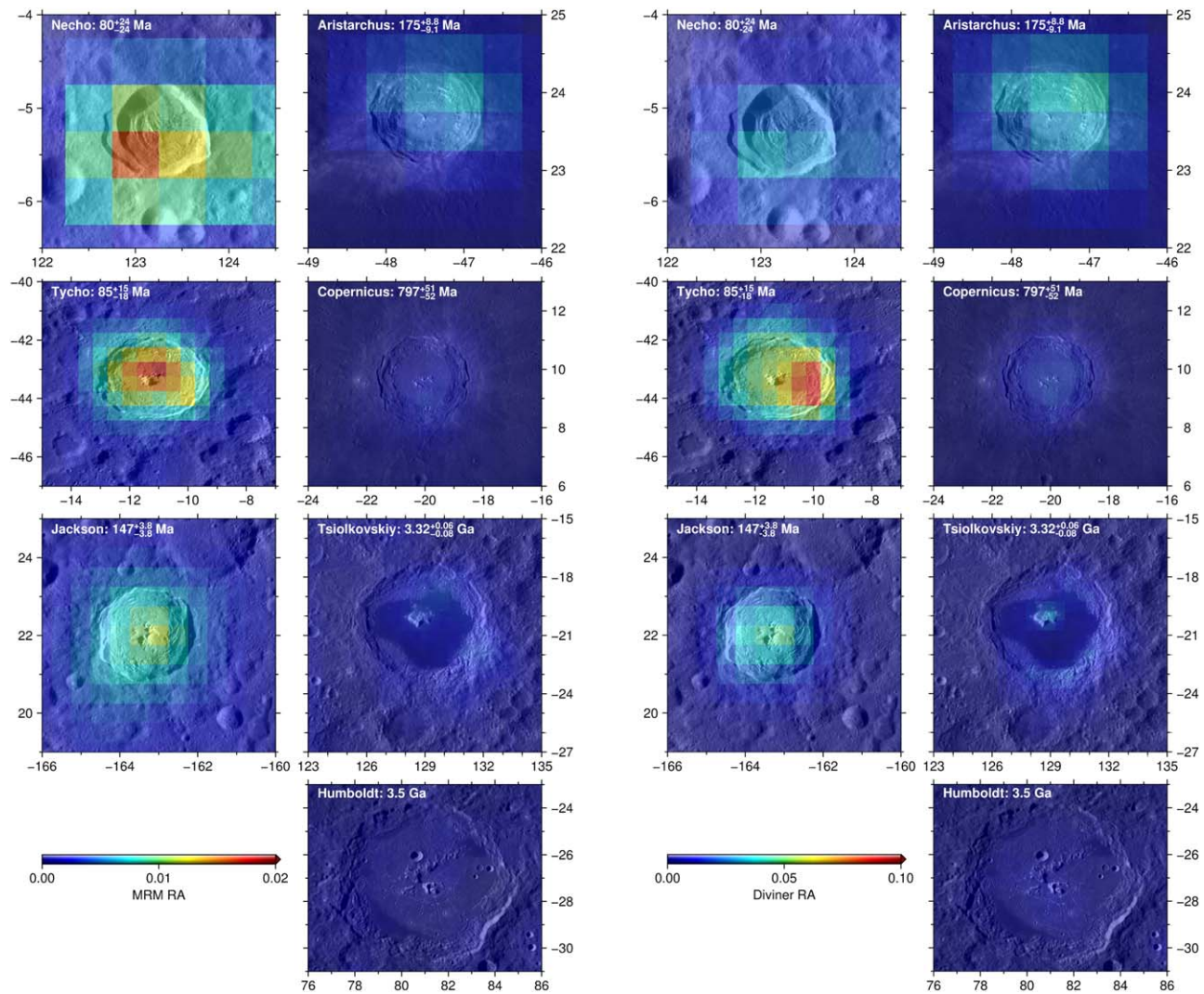


Figure 19. Rock concentration at different craters. The left two columns are retrieved MRM RA and the right two columns are Diviner RA from Bandfield et al. (2011). The WAC images are used as mosaics. Note that crater ages are given based on published model ages.

indicate different geological processes and rock destructions—for example, impact melts flow (debris transportation and/or deposition), micro-meteorites impact (sandblasting effect), and the overturn history of regolith.

We also attempted to map d_{rock} versus age base on the two kinds of RA values. However, we find that there are dramatically elevated d_{rock} values covering the surrounding

of the craters which are contrary to the distribution of MRM RA and Diviner RA. We suppose that this is caused by the lack of large rocks but the existence of small rocks that are smaller than ~ 1 m in diameter (the threshold of Diviner RA). These rocks contribute to MRM RA but are not considered in Diviner rock retrieval technique which results in large ratio of $RA_{\text{MRM}}/RA_{\text{Diviner}}$. Therefore, the d_{rock} should be cautiously

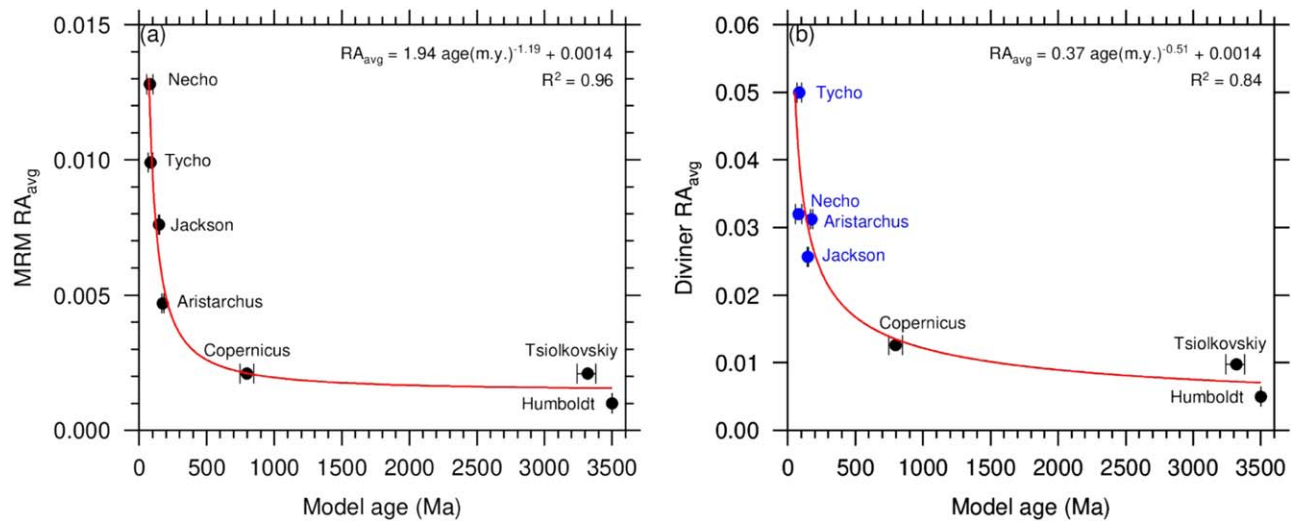


Figure 20. The averaged (a) MRM RA and (b) Diviner RA vary as a function of age for studied craters. The error bars denote the age uncertainties. The red line is the best fit. Note that the blue dots in (b) indicate the averaged Diviner RA do not decrease with age within 1 Ga.

used unless most of rocks are larger than ~ 1 m that will be meaningful in geology interpretations.

To quantify the degradation of rocky craters, we plot the averaged MRM RA (RA_{avg}) versus the age of each crater (Figure 20(a)). This provides a new empirical estimate for the time-dependent rate of rock breakdown and dating the degradation of lunar craters.

Note that the mechanical breakdown of rocks is the dominant process by which lunar blocks and/or fragments are transformed into low-density, fine-grained regolith material (Hörz & Cintala 1997). The developing regolith layer covers the residual rocks and masks their thermophysical signature (Bandfield et al. 2011; Neish et al. 2013; Ghent et al. 2014). The best-fit power law (red line), $RA_{\text{avg}} = 1.94 \times (\text{age}[\text{m.y.}])^{-1.19} + 0.0014$, indicates that near-surface rock concentration decreases rapidly within the first ~ 1 Ga.

For older craters (>1 Ga), the MRM RA_{avg} varies slowly with age, indicating that subsurface rock breakdown from micrometeorite is greatly reduced by the low-impedance surface layer (Stickle & Schultz 2012). Radar observations also confirm that the subsurface rocks can remain undisturbed by surface processes for >3 Ga (Ghent et al. 2016), which supports these findings.

However, the Diviner RA_{avg} shown in Figure 20(b) does not present a good degradation trend for these young craters (blue dots). For example, Tycho and Aristarchus are, respectively, older than Necho and Jackson, but they have more exposed rocks, which brings uncertainties to evaluate the crater degradation. This might be caused by their different impact history (excavation, melt flow, debris deposition, etc.) and latter micrometeorite bombardments. Additionally, the buried rocks will not be breakdown and form regolith rapidly in these short periods (80–175 Ma, as can be seen in Figure 19). Therefore, both exposed and buried rocks should be included to quantify the degradation of craters. And the MRM RA retrieved in this study is better to investigate the crater degradation and regolith evolution of the Moon.

5. Conclusion

Rocks are formed by the impact gardening and micrometeorite bombardment that reworks the surface of the Moon.

For several billion years, rocks have been destroyed by sandblasting from much smaller impactors and by catastrophic rupture by impactors of comparable sizes (Ghent et al. 2014). Considering that the lunar near-surface material is mixed evenly with rocks and soils, we employed the Diviner thermal data as surface thermal constraints and retrieved the RA at several craters and highland areas based on CE-2 microwave data at 7.8 and 19.35 GHz. Here, the rock concentration is represented by volumetric percentage at each bin.

The retrieved rock concentration agrees well with the hummocky regions of the Tycho crater and the impact melts at Tycho's antipode. Neglecting the small rocks (<1 m in diameter) that cannot be sensed by Diviner rock retrieval technique, we defined the equivalent rock thickness (d_{rock}) at each bin, i.e., the MRM rock concentration was divided by the corresponding Diviner RA. We found that large values of d_{rock} —for example at the Aristarchus crater—correlates with more rocks and/or small fragments that are mantled by lava flows. Furthermore, small values of d_{rock} correlate with rocks exposed at the lunar surface, which can be sensed by both MRM and Diviner rock models.

Based on the published model ages of seven large craters, we compared the rock distribution to crater age. To quantify the degradation of these craters, we plotted the maximum rock concentration of each crater versus the model age. The result showed that the rock concentration decreased rapidly within 1 Ga after the impact event. This is mainly caused by the breakdown of exposed rocks and the maturation of surface materials. However, for older craters (>1 Ga), the rock concentrations decrease slowly with increasing ages. This indicates that the rocks residing at greater depths can be shielded from destructive geological processes such as micrometeorite bombardment.

The authors thank Matt Siegler at Planetary Science Institute and a second anonymous reviewer for constructive comments that significantly improved the quality of the manuscript. G.W. was supported by the B-type Strategic Priority Program of the Chinese Academy of Sciences (No. XDB 41000000) and National Natural Science Foundation of China (No. 41803052, 41931077). The Diviner T_{BoI} data set and Diviner rock

abundance data were obtained from the NASA Planetary Data System Geosciences Node, available at <http://pds-geosciences.wustl.edu/missions/lro/diviner.htm>. CE-2 microwave radiometer data were provided by the Ground Research and Application System of Chinese Lunar Exploration Program and are available online (<http://moon.bao.ac.cn>).

ORCID iDs

Guangfei Wei  <https://orcid.org/0000-0002-3586-2300>

Shane Byrne  <https://orcid.org/0000-0002-6735-4685>

References

- Bandfield, J. L., Cahill, J. T. S., Carter, L. M., et al. 2017, *Icar*, **283**, 282
- Bandfield, J. L., Ghent, R. R., Vasavada, A. R., et al. 2011, *JGR*, **116**, E00H02
- Basilevsky, A., Head, J., & Horz, F. 2013, *P&SS*, **89**, 118
- Bergman, D. J. 1978, *PhR*, **43**, 377
- Bray, V. J., Tornabene, L. L., Keszthelyi, L. P., et al. 2010, *GeoRL*, **37**, L21202
- Cahill, J. T., Thomson, B., Patterson, G. W., et al. 2014, *Icar*, **243**, 173
- Campbell, B. A. 2012, *JGR*, **117**, E06008
- Campbell, B. A., Carter, L. M., Campbell, D. B., et al. 2010, *Icar*, **208**, 565
- Campbell, B. A., Carter, L. M., Hawke, B. R., Campbell, D. B., & Ghent, R. R. 2008, *Geo*, **36**, 135
- Campbell, M. J., & Ulrichs, J. 1969, *JGR*, **74**, 5867
- Carrier, W. D., Olhoeft, G. R., & Mendell, W. 1991, in *Lunar Source Book: A User's Guide to the Moon*, ed. G. H. Heiken, D. T. Vaniman, & B. M. French (New York: Cambridge Univ. Press), 475
- Carter, L. M., Neish, C. D., Bussey, D. B. J., et al. 2012, *JGRE*, **117**, E00H09
- Chan, K. L., Tsang, K. T., Kong, B., & Zheng, Y.-C. 2010, *E&PSL*, **295**, 287
- Dhingra, D., Head, J. W., & Pieters, C. M. 2017, *Icar*, **283**, 268
- Dundas, C. M., & McEwen, A. S. 2007, *Icar*, **186**, 31
- Elder, C. M., Hayne, P. O., Bandfield, J. L., et al. 2017, *Icar*, **290**, 224
- Feng, J., Siegler, M. A., & Hayne, P. O. 2020, *JGRE*, **125**, e2020JE006405
- Feng, J., Siegler, M. A., Hayne, P. O., & Blewett, D. T. 2019, *LPI*, **50**, 3176
- Feng, J., SU, Y., Liu, J., et al. 2013, *J. China Univ. Geosci.: Earth Science*, **38**, 898
- Ghent, R. R., Carter, L. M., Bandfield, J. L., Udovicic, C. J. T., & Campbell, B. A. 2016, *Icar*, **273**, 182
- Ghent, R. R., Hayne, P. O., Bandfield, J. L., et al. 2014, *Geo*, **42**, 1059
- Gong, X., & Jin, Y.-Q. 2013, *AcAau*, **86**, 237
- Greenhagen, B. T., Neish, C. D., Bandfield, J. L., et al. 2013, *LPI*, **44**, 2987
- Greenhagen, B. T., Neish, C. D., Williams, J.-P., et al. 2016, *Icar*, **273**, 237
- Hawke, B. R., & Head, J. W. 1977, in *Impact and Explosion Cratering: Planetary and Terrestrial Implications*, ed. D. J. Roddy, R. O. Pepin, & R. B. Merrill (New York: Pergamon), 815
- Hayne, P. O., Bandfield, J. L., Siegler, M. A., et al. 2017, *JGRE*, **122**, 2371
- Horai, K.-I., & Simmons, G. 1972, *PrAA*, **28**, 243
- Hörz, F., & Cintala, M. 1997, *M&PS*, **32**, 179
- Hu, G., Chan, K. L., Zheng, Y., & Xu, A. 2018, *ITGRS*, **56**, 5471
- Hu, G.-P., Chan, K. L., Zheng, Y.-C., Tsang, K. T., & Xu, A.-A. 2017, *Icar*, **294**, 72
- Klem, S. M., Henriksen, M. R., Stopar, J., et al. 2014, *LPI*, **45**, 2885
- Krüger, T., van der Bogert, C., & Hiesinger, H. 2016, *Icar*, **273**, 164
- Lawrence, D. J., Feldman, W. C., Elphic, R. C., et al. 2002, *JGR*, **107**, 5130
- Li, Y., & Wu, B. 2018, *JGRE*, **123**, 1061
- Martinot, M., Besse, S., Flahaut, J., et al. 2018, *JGRE*, **123**, 612
- Mazarico, E., Rowlands, D. D., Neumann, G. A., et al. 2012, *JGeod*, **86**, 193
- McEwen, A. S., Robinson, M. S., Eliason, E. M., et al. 1994, *Sci*, **266**, 1858
- Mendell, W. W. 1976, in *Proc. Lunar Sci. Conf. 7th* (New York: Pergamon Press), 2705
- Neish, C. D., Greenhagen, B. T., Patterson, G. W., et al. 2013, *LPI*, **44**, 1585
- Nozette, S., Spudis, P., Bussey, B., et al. 2010, *SSRv*, **150**, 285
- Paige, D. A., Curren, I., Russell, P., Moon, S., & Boyd, A. 2018, *EPSC*, **12**, 603
- Paige, D. A., Foote, M. C., Greenhagen, B. T., et al. 2010a, *SSRv*, **150**, 125
- Paige, D. A., Siegler, M. A., & Zhang, J. A. 2010b, *Sci*, **330**, 479
- Robinson, M., Thomas, P., Plescia, J., et al. 2016, *Icar*, **273**, 121
- Robinson, M. S., Brylow, S. M., Tschimmel, M., et al. 2010, *SSRv*, **150**, 81
- Robinson, M. S., Thomas, P. C., Tran, T., et al. 2011, *LPI*, **42**, 2511
- Roelof, E. C. 1968, *Icar*, **8**, 138
- Sato, H., Robinson, M. S., Lawrence, S. J., et al. 2017, *Icar*, **296**, 216
- Siegler, M. A., Feng, J., Lucey, P., et al. 2019, *LPI*, **50**, 3151
- Stickle, A. M., & Schultz, P. H. 2012, *JGR*, **117**, E07006
- Sturm, S., Kenkmann, T., Willmes, M., P'osges, G., & Hiesinger, H. 2015, *M&PS*, **50**, 141
- Taylor, G. J., Warren, P., Ryder, G., et al. 1991, in *Lunar Source Book: A User's Guide to the Moon*, ed. G. H. Heiken, D. T. Vaniman, & B. M. French (New York: Cambridge Univ. Press), 183
- Thompson, T. W., Masursky, H., Shorthill, R. W., Tyler, G. L., & Zisk, S. H. 1974, *Moon*, **10**, 87
- Vasavada, A. R., Bandfield, J. L., Greenhagen, B. T., et al. 2012, *JGRE*, **117**, E00H18
- Wang, Z., Li, Y., Jiang, J., & Li, D. 2010a, *ScChD*, **53**, 1365
- Wang, Z., Li, Y., Zhang, X., et al. 2010b, *ScChD*, **53**, 1392
- Wei, G., Li, X., Gan, H., et al. 2019, *JGRE*, **124**, 1433
- Williams, J. P., Paige, D. A., Greenhagen, B. T., & Sefton-Nash, E. 2017, *Icar*, **283**, 300
- Woodhouse, I. H. 2007, *Introduction to Microwave Remote Sensing* (Boca Raton, FL: CRC Press)
- Zheng, Y.-C., Chan, K. L., Tsang, K. T., et al. 2019, *Icar*, **319**, 627
- Zheng, Y. C., Tsang, K. T., & Chan, K. L. 2012, *Icar*, **219**, 194
- Zhu, Y., Zheng, Y., Fang, S., Zou, Y., & Pearson, S. 2019, *AdSpR*, **63**, 750